

# H<sub>2</sub> chemistry in galaxy simulations: an improved supernova feedback model

Alessandro Lupi<sup>1</sup>★

<sup>1</sup>*Sorbonne Universités, UPMC Univ Paris 6 et CNRS, UMR 7095, Institut d’Astrophysique de Paris, 98 bis bd Arago, F-75014 Paris, France*

Draft 2 June 2022

## ABSTRACT

In this study, we present a new, physically motivated sub-grid prescription for supernova feedback, which accounts for the unresolved energy-conserving phase of the bubble expansion. We implement this model in the mesh-less hydrodynamic code GIZMO, coupled with the chemistry library KROME, and we validate it against different setups, to address how it affects the formation/dissociation of molecular hydrogen (H<sub>2</sub>). First, we test the model in very idealised conditions, to show that it can accurately reproduce the terminal momentum of the blast-wave independent of resolution. Then, we apply it to a suite of numerical simulations of an isolated Milky Way-like galaxy and compare it with a similar run employing the delayed-cooling sub-grid prescription. We find that the delayed-cooling model, by pressurising ad-hoc the gas, is more effective in suppressing star formation. However, to get this effect, it must maintain the gas warm/hot at densities where it is expected to cool efficiently, artificially changing the thermo-chemical state of the gas, and reducing the H<sub>2</sub> abundance even in dense gas. Mechanical feedback, on the other hand, is able to reproduce observed correlations like the Kennicutt–Schmidt relation and the H<sub>2</sub> column densities without altering the gas thermodynamics, and, at the same time, can drive more powerful outflows. Finally, we show that the model is consistent at different resolution levels, with only mild differences.

**Key words:** ISM: molecules - galaxies: ISM - galaxies: formation - galaxies: evolution.

## 1 INTRODUCTION

According to the current cosmological model, baryons cool down and fall within the potential well of dark matter haloes, fragmenting and forming stars (and galaxies). From simple arguments, star formation (SF) should occur on a free-fall time-scale, consuming very quickly all the available gas supply (e.g., Bournaud et al. 2010; Dobbs et al. 2011). However, the typical observed time-scale for SF is much longer than that expected from these simple arguments.

One of the possible reasons behind this difference is stellar feedback, which evacuates the gas from the SF sites, suppressing the actual SF efficiency. One of the most important feedback processes to be considered is supernova (SN) feedback, i.e. the explosion of massive stars ( $M_s > 8 M_\odot$ ) and accreting white dwarfs in binary systems (as type Ia SNe).

Although a proper description of the SN explosion mechanism is still missing, at pc scales SN events can be simply modelled as an instantaneous injection of mass, metals, and energy into the surrounding medium. In the last

few decades, many authors investigated the evolution of the SN-driven bubble, with both analytical calculations and numerical simulations (e.g., Chevalier 1974; McKee & Ostriker 1977; Cioffi et al. 1988; Kim & Ostriker 2015; Martizzi et al. 2015; Geen et al. 2016). Unfortunately, to properly capture this evolution in numerical simulations, in particular the initial energy-conserving phase (the Sedov–Taylor phase; Taylor 1950a,b; Sedov 1959), when radiative losses are still unimportant, extreme mass and spatial resolutions are needed. Unfortunately, this is currently not achievable in galaxy-scale simulations, and it gets even worse in cosmological ones. In this case, a simple thermal energy injection would result in efficient radiative losses and a negligible feedback effect, hence ad-hoc sub-grid prescriptions are necessary to overcome this problem.

At very low resolution, when the inter-stellar medium (ISM) is unresolved, empirical models are usually employed, like in (i) Navarro & White (1993), where energy is injected in the kinetic form, (ii) Springel & Hernquist (2003); Keller et al. (2014), where the gas is described via a sub-grid multi-phase model, (iii) Stinson et al. (2006), where cooling is shut off for some time to allow the blast-wave to expand follow-

★ E-mail: lupi@iap.fr

ing the energy-conserving solution, and (iv) [Dalla Vecchia & Schaye \(2012\)](#), where many SN events are stochastically grouped together to produce more energetic explosions.

Despite the success of these models, at higher resolution, when the multi-phase structure of the ISM can be resolved, a more physically motivated model is desirable. Recently, several authors put an effort to implement a new sub-grid supernova feedback model, so-called mechanical feedback, in different hydrodynamic codes ([Hopkins et al. 2013](#); [Kimm & Cen 2014](#); [Smith et al. 2018](#); [Hopkins et al. 2018b](#)), where the feedback deposition takes into account the possibly unresolved Sedov–Taylor phase, injecting 1) the initial ejecta momentum/thermal energy if this phase is resolved, or 2) the terminal momentum of the bubble otherwise.

Recently, [Martizzi et al. \(2015\)](#) investigated the evolution of SN bubbles in homogeneous and inhomogeneous media with very high resolution, in order to properly model the Sedov–Taylor phase. With their simulations, the authors were able to fit an analytic formula to properly describe the thermal energy and the momentum of the SN bubble at different stages of the evolution. This prescription, so far implemented only by [Semenov et al. \(2017\)](#), allows a more accurate estimation of the amount of thermal energy and momentum to be injected as a function of the ‘coupling radius’, i.e. the resolution of the simulation.

Here, we implement the same prescription in the numerical code GIZMO ([Hopkins 2015](#)), and we validate it against different tests, i.e. a single explosion in a uniform medium, and an isolated galaxy. For the first time, we follow the evolution of a single galaxy with on-the-fly non-equilibrium chemistry of  $H_2$  and a physically motivated SN feedback, to assess whether the correlation between  $H_2$  and star formation rate (SFR) surface densities can still be naturally reproduced without assuming a priori dependence of SF on the  $H_2$  abundance ([Lupi et al. 2018](#)).

The manuscript is organised as follows: in Section 2, we describe the model and its implementation in the code; in Section 3 we validate it by means of a single SN explosion test in a pseudo-uniform medium; in Section 4, we describe the sub-grid model employed in the galaxy simulations; in Section 5, we present our results; in Section 6, we discuss the limits of the model and we draw our conclusions.

## 2 MECHANICAL FEEDBACK MODEL

### 2.1 The hydrodynamic code gizmo

GIZMO ([Hopkins 2015](#)), descendant from GADGET3, itself descendant from GADGET2 ([Springel 2005](#)), implements a new method to solve hydrodynamic equations, aimed at capturing the advantages of both usual techniques used so far, i.e. the Lagrangian nature of smoothed particle hydrodynamics codes, and the excellent shock-capturing properties of Eulerian mesh-based codes, and at avoiding their intrinsic limits. The code uses a volume partition scheme to sample the volume, which is discretised amongst a set of tracer ‘particles’ which correspond to unstructured cells. Unlike moving-mesh codes (e.g. AREPO; [Springel 2010](#)), the effective volume associated to each cell is not defined via a Voronoi tessellation, but is computed in a kernel-weighted fashion. Hydrodynamic equations are then solved across the ‘effective’

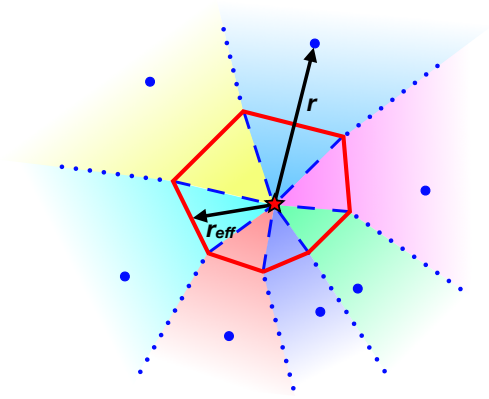


**Figure 1.** Coupling scheme for the mechanical SN feedback. The red lines correspond to a convex hull around the stellar particle, with each line representing an effective face shared with a gas cell. The dotted (dashed) lines correspond to the separation between the volumes associated to each gas neighbour, outside (inside) the convex hull built around the star. All the separation lines between particle pairs (including the stars) are obtained here from a Voronoi tessellation, that is similar to the result obtained in GIZMO. Each neighbour receives an amount of momentum proportional to the renormalised vector weight, computed from the solid angle subtended by the face. The arrow identified with  $r$  represents the coupling radius used to compute the bubble expansion solution, whereas that identified with  $r_{\text{eff}}$  corresponds to the effective distance used to prevent unphysical kicks to particles whose face is outside the maximum extension radius of the bubble for very-low density medium.

faces amongst the cells using a Godunov-like method, like in standard mesh-based codes. In these simulations, we employ the mesh-less finite-mass method, where particle masses are preserved, and the standard cubic-spline kernel, setting the desired number of neighbours to 32. Gravity is based on a Barnes-Hut tree, as in GADGET3 and GADGET2. It provides two different softening schemes, fixed and adaptive, for all particles. While a fixed gravitational softening can be a reasonable assumption for dark matter and stars, gas is volume-filling, hence adaptive softenings represent a better choice. Moreover, adaptive softenings ensure that both hydrodynamics and gravity are computed assuming the same mass distribution within the kernel, ensuring that the force is always Newtonian.

### 2.2 Neighbour search and coupling

We describe here the basic assumptions in our mechanical feedback model. When a SN explodes, we must couple energy (and/or momentum) and mass (and metals) to the surrounding medium in a conservative way. Unlike in mesh-based codes, where the volume is perfectly sampled, and the coupling is almost straightforward, the coupling in particle-based codes like GIZMO requires more care.

In our model, we follow the approach proposed in [Hopkins et al. \(2018a\)](#), finding an effective number of neighbours around every star particle as  $N_{\star} = 4\pi/3h_s^3n_s^3$ , where  $n_s = \sum_j W(\mathbf{x}_{j,s}, h_s)$ ,  $W$  is the kernel function,  $\mathbf{x}_{j,s} = \mathbf{x}_j - \mathbf{x}_s$

is the particle separation vector, and  $h_s$  is the star kernel size. In order to guarantee that the area around the star is covered, we determine  $h_s$  by requiring  $N_\star = 64$ . As stated in Hopkins et al. (2018a), to better couple the feedback with the gas, instead of distributing it to the gas within the kernel of the star only, we also consider all gas particles with their kernel encompassing the star, i.e.  $|\mathbf{x}_{j,s}| < h_j$ , with  $j$  representing the  $j$ -th particle.

After having identified the neighbours, we estimate the fraction  $\omega_j$  of energy/momentum and mass each neighbour should receive, as the normalised solid angle subtended by the gas element around the star. This is done by building a set of effective faces shared between star and gas with some convex hull, as shown in Fig. 1. Analytically, we can write

$$\omega_j = \frac{\Delta\Omega_j}{4\pi} = \frac{1}{2} \left( 1 - \frac{1}{\sqrt{1 + \mathbf{A}_j \cdot \mathbf{x}_{j,s}/(\pi|\mathbf{x}_{j,s}|^3)}} \right), \quad (1)$$

where  $\mathbf{A}_j$  is the effective face area, which goes from  $\omega_j \approx 1/2$  for  $|\mathbf{x}_{j,s}|^2 \ll A_j$  to  $\omega_j \approx A_j/(4\pi|\mathbf{x}_{j,s}|^2)$  for  $|\mathbf{x}_{j,s}|^2 \gg A_j$ . Although different ways of constructing a convex hull exist, we follow Hopkins et al. (2018a) and use<sup>1</sup>

$$\mathbf{A}_j = \left\{ n_j^{-2} \frac{\partial W(\mathbf{x}_{j,s}, h_j)}{\partial |\mathbf{x}_{j,s}|} + n_s^{-2} \frac{\partial W(\mathbf{x}_{j,s}, h_s)}{\partial |\mathbf{x}_{j,s}|} \right\} \cdot \frac{\mathbf{x}_{j,s}}{|\mathbf{x}_{j,s}|}. \quad (2)$$

However, since we also inject momentum in the surroundings, we must guarantee that linear momentum is conserved. To do so, we impose a *tensor* renormalisation, where the six-dimensional weights  $\hat{\mathbf{x}}_{j,s}^\pm$  are defined as

$$\hat{\mathbf{x}}_{j,s} = \frac{\mathbf{x}_{j,s}}{|\mathbf{x}_{j,s}|} = \sum_{+,-} \hat{\mathbf{x}}_{j,s}^\pm \quad (3)$$

$$(\hat{\mathbf{x}}_{j,s}^+)^k = |\mathbf{x}_{j,s}|^{-1} \max(\mathbf{x}_{j,s}^k, 0) \Big|_{k=x,y,z} \quad (4)$$

$$(\hat{\mathbf{x}}_{j,s}^-)^k = |\mathbf{x}_{j,s}|^{-1} \min(\mathbf{x}_{j,s}^k, 0) \Big|_{k=x,y,z}. \quad (5)$$

We can therefore derive the actual weight as

$$\tilde{\mathbf{w}}_j = \frac{\mathbf{w}_j}{\sum_i |\mathbf{w}_i|} \quad (6)$$

$$\mathbf{w}_j = \omega_j \sum_{+,-} \sum_k (\hat{\mathbf{x}}_{j,s}^\pm)^k f_\pm^k \quad (7)$$

$$(f_\pm)^k = \left\{ \frac{1}{2} \left[ 1 + \left( \frac{\sum_i \omega_i |\hat{\mathbf{x}}_{j,s}^\mp|^k}{\sum_i \omega_i |\hat{\mathbf{x}}_{j,s}^\pm|^k} \right)^2 \right] \right\}^{1/2}. \quad (8)$$

With this definition, we guarantee the right distribution of energy/momentum, mass, and metals and, at the same time, we ensure that the total linear momentum vector vanishes in the reference system of the star.

<sup>1</sup> We note that, when either  $s$  or  $j$  are outside the kernel of the other particle ( $W=0$ ), this definition results in a constant area  $\mathbf{A}_j$  that only depends on the properties of the particle with the largest kernel. For instance, in the extreme case of low density around the star, with all the gas neighbours having  $h_j < |\mathbf{x}_{j,s}|$  and  $h_i \gg h_j$ , this equation assigns equal weights to all the gas neighbours of the star, without taking into account their actual volume. In these cases, we employ an alternative definition of the effective area, i.e.  $\mathbf{A}_j = \frac{1}{n_i n_j} \left\{ \frac{\partial W(\mathbf{x}_{j,s}, h_j)}{\partial |\mathbf{x}_{j,s}|} + \frac{\partial W(\mathbf{x}_{j,s}, h_s)}{\partial |\mathbf{x}_{j,s}|} \right\} \cdot \frac{\mathbf{x}_{j,s}}{|\mathbf{x}_{j,s}|}$ .

We can now define the fractional quantities each neighbour receives as  $\Delta m_j = |\tilde{\mathbf{w}}_j| m_{\text{ej}}$ ,  $\Delta m_{Z,j} = |\tilde{\mathbf{w}}_j| m_{Z,\text{ej}}$ ,  $\Delta E_j^* = |\tilde{\mathbf{w}}_j| E_{\text{SN}}$ , and  $\Delta \mathbf{p}_j^* = \tilde{\mathbf{w}}_j p_{\text{SN}}$ . Here,  $m_{\text{ej}}$  is the ejecta mass,  $m_{Z,\text{ej}}$  is the metal mass in the ejects,  $E_{\text{SN}}$  is the energy injected by the SN, and  $p_{\text{SN}}$  the injected momentum.

So far, all the quantities we used were defined in the reference frame of the star ( $S^*$ ). However, in a real galaxy, both stars and gas are in motion. In order to account for the gas-star relative motion and conserve both energy and momentum, we first move to the reference frame moving with the gas cell  $S'$ , and compute the pre-shock properties of the ejecta. The coupled mass and the metal mass are not affected by the boost, whereas the new ejecta momentum and energy become  $\Delta \mathbf{p}'_j = \Delta \mathbf{p}_j^* + \Delta m_j (\mathbf{v}_s - \mathbf{v}_j)$ , and  $\Delta E'_j = \Delta E_j^* + \frac{1}{2\Delta m_j} (|\Delta \mathbf{p}'_j|^2 - |\Delta \mathbf{p}_j^*|^2)$ , respectively, where  $\mathbf{v}_j$  is the gas velocity in the lab/simulation frame  $S$ . Now, we can update the  $j$ -th neighbour properties in  $S'$  as

$$\mathbf{p}'_j^{\text{new}} = \Delta \mathbf{p}'_j \quad (9)$$

$$E_j^{\text{new}} = E'_j + \Delta E'_j. \quad (10)$$

Finally, we move back to the lab/simulation reference frame, where the new properties are written as

$$m_j^{\text{new}} = m_j + \Delta m_j \quad (11)$$

$$m_{Z,j}^{\text{new}} = Z_j^{\text{new}} m_j^{\text{new}} = Z_j m_j + \Delta m_{Z,j} \quad (12)$$

$$\mathbf{p}_j^{\text{new}} = m_j^{\text{new}} \mathbf{v}_j + \Delta \mathbf{p}'_j = \mathbf{p}_j + \Delta \mathbf{p}_j^* + \Delta m_j \mathbf{v}_s \quad (13)$$

$$E_j^{\text{new}} = E'_j + \Delta E'_j + \frac{1}{2m_j^{\text{new}}} (|\mathbf{p}_j^{\text{new}}|^2 - |\mathbf{p}_j^{\text{new}*}|^2) \quad (14)$$

In  $S'$ , the pre-coupling total energy simply corresponds to  $E'_j = U_j$ , where  $U_j$  is the gas cell internal energy. The updated internal energy of the gas cell in  $S$  directly follows from the after-coupling total energy and momentum as

$$U_j^{\text{new}} = E_j^{\text{new}} - \frac{1}{2m_j^{\text{new}}} |\mathbf{p}_j^{\text{new}}|^2 = U_j + \Delta E'_j - \frac{1}{2m_j^{\text{new}}} |\Delta \mathbf{p}'_j|^2 \quad (15)$$

where  $\Delta E'_j - |\Delta \mathbf{p}'_j|^2/(2m_j^{\text{new}}) \equiv \Delta U_j$ .

### 2.3 The unresolved energy-conserving phase

When resolution is low, the energy-conserving phase of the SN bubble expansion cannot be resolved. This inevitably leads to a quick loss of thermal energy due to radiative cooling, and a reduced effect of SN feedback. To avoid this, we account for the momentum gained during the unresolved phase as resulting from high-resolution simulations of single SNe. In particular, we follow Martizzi et al. (2015), and we rewrite the thermal energy and the momentum in terms of the swept mass  $m_{\text{swept}}$ , as

$$\begin{aligned} E_{\text{th}}(m_{\text{swept}}) &= \begin{cases} E_{\text{th,ej}} & m_{\text{swept}} \leq m_{\text{cool}} \\ E_{\text{th,ej}} \left( \frac{\min\{m_{\text{swept}}, m_r\}}{m_{\text{cool}}} \right)^{-\alpha/3} & m_{\text{swept}} > m_{\text{cool}} \end{cases} \\ p(m_{\text{swept}}) &= p_0 \left( \frac{\min\{m_{\text{swept}}, m_{\text{cool}}\}}{m_{\text{ej}}} \right)^{0.5}, \end{aligned} \quad (16)$$

where, assuming an homogeneous medium with initial density  $\rho_0$ ,  $m_{\text{cool}} = 4/3\pi\rho_0 r_{\text{cool}}^3$ , with  $r_{\text{cool}}$  the cooling radius,  $\alpha$

is the declining slope for the thermal energy outside  $r_{\text{cool}}$ , and  $m_r = 4/3\pi\rho_0 r_r^3$  is the mass corresponding to the radius  $r_r$  after which the thermal energy is roughly constant.<sup>2</sup>  $E_{\text{th,ej}}$  is the thermal energy during the Sedov–Taylor phase (corresponding to  $\sim 0.69 E_{\text{ej}}$ ), and  $p_0 = \sqrt{2m_{\text{ej}}E_{\text{ej}}}$  is the ejecta momentum, with  $E_{\text{ej}} \equiv \Delta E'$ .

According to [Haid et al. \(2016\)](#), in the case of an inhomogeneous medium, the differences from the homogeneous case can be captured by considering each gas element separately, and determining the solution of the homogeneous case using the gas element properties. Following this approach, we can determine the right solution independently for each ‘cone’ (see Fig. 1) by using the  $j$ -particle density and metallicity to estimate  $\alpha$ ,  $R_{\text{cool}}$ , and  $R_r$  as ([Martizzi et al. 2015](#))

$$\begin{aligned} \alpha &= 7.8 \left(\frac{Z}{Z_\odot}\right)^{+0.050} \left(\frac{n_{\text{Htot}}}{100 \text{ cm}^{-3}}\right)^{+0.030}, \\ r_{\text{cool}} &= 3.0 \left(\frac{Z}{Z_\odot}\right)^{-0.084} \left(\frac{n_{\text{Htot}}}{100 \text{ cm}^{-3}}\right)^{-0.42} \text{ pc}, \\ r_r &= 5.5 \left(\frac{Z}{Z_\odot}\right)^{-0.074} \left(\frac{n_{\text{Htot}}}{100 \text{ cm}^{-3}}\right)^{-0.40} \text{ pc}, \end{aligned} \quad (17)$$

where  $n_{\text{Htot}}$  is the total number density of hydrogen nuclei and  $\rho_0 = n_{\text{Htot}}/X * m_{\text{H}}$ , with  $X = 0.76$  the Hydrogen nuclei fraction and  $m_{\text{H}}$  the Hydrogen mass. Using Eq. (16) and assuming  $m_{\text{swept}} = m_{\text{ej}} + \min\{4/3\pi\rho_j|\mathbf{x}_{j,s}|^3, m_j/|\tilde{\mathbf{w}}_j|\}$ , we can estimate  $\Delta U_j = E_{\text{th}}(m_{\text{swept}})$  and  $\Delta \mathbf{p}'_j = p(m_{\text{swept}})/p_0 \Delta \mathbf{p}'_j$ , where  $\Delta \mathbf{p}'_j$  replaces  $\Delta \mathbf{p}'_j$  in Eq. (13).

Although the model well captures the unresolved Sedov–Taylor phase and can reproduce the terminal momentum, as we will show in the next section, there are some cases where some neighbours can be far away from the star, well beyond the radius at which the bubble should merge with the ISM even at very low densities. Previous studies have shown that when the bubble comes into pressure balance with the ISM, it stops expanding (e.g. [McKee & Ostriker 1977](#); [Cioffi et al. 1988](#)), leaving a hot, low-density cavity which is later encroached upon by the surrounding gas. However, for very-low density gas ( $n_{\text{Htot}} \lesssim 0.01 \text{ cm}^{-3}$ ; [Cioffi et al. 1988](#)), the pressure balance is reached when the bubble is still in the energy-conserving phase and, in these cases, the coupling scheme can fail, injecting too much momentum. To prevent such a behaviour, we limit the momentum coupling to the neighbours with  $\rho_j > \rho_{\text{cr}} = 0.005 m_{\text{H}} \text{ cm}^{-3}$ , and for which the distance of the effective face shared with the star  $r_{\text{eff}} < R_{\text{max}}$ , where  $R_{\text{max}} = 600 \text{ pc}$  is the merging radius for  $\rho_g = \rho_{\text{cr}}$  and  $T = 10^4 \text{ K}$  ([Cioffi et al. 1988](#)),<sup>3</sup> and  $r_{\text{eff}} = \max\{|\mathbf{x}_{j,s}| - L_j, 0\}$ ,

<sup>2</sup> We notice that the equations in [Martizzi et al. \(2015\)](#) are slightly different from those employed here. First, instead of  $m_{\text{ej}}$ , there is a scale radius  $r_0$ , used to extrapolate the momentum at small radii, corresponding to a scale mass  $m_0 = 4/3\pi\rho_0 r_0^3$ . However, the use of  $m_0$  introduces an additional dependence of the terminal momentum on the initial ejecta momentum, which is not observed in similar studies of single SN explosions. Our choice removes this dependence. Second, in [Martizzi et al. \(2015\)](#), the terminal momentum is reached at a radius  $R_b > R_{\text{cool}}$ . We performed several experiments and we found that, in our case,  $R_{\text{cool}}$  was a better choice (see Section 3) to reproduce the high-resolution simulations.

<sup>3</sup> The value for  $R_{\text{max}}$  has been derived from Eqs. (3.33a) and

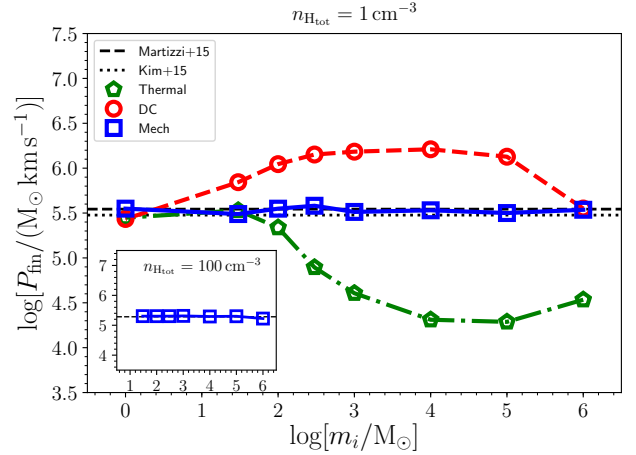


**Figure 2.** Convergence test of the mechanical SN feedback model, via a single SN explosion in a pseudo-homogeneous medium with  $n_{\text{Htot}} = 1 \text{ cm}^{-3}$  (main panel) and  $n_{\text{Htot}} = 100 \text{ cm}^{-3}$  (inset). We show the terminal momentum as a function of mass resolution ( $m_i$ ). The black dashed line corresponds to the terminal momentum as estimated using Eq. (16), and the black dotted one to the terminal momentum from [Kim & Ostriker \(2015\)](#). The mechanical feedback case is shown as a solid blue line (and the blue squares). As a comparison, we also show with a green dot-dashed line (and the green pentagons) the fully thermal case, and with the red dashed line (and the red circles) the delayed-cooling case. Our model can accurately reproduce the terminal momentum independent of the resolution, both at the typical densities of SF sites (in the inset) and in the ISM (main panel).

with  $L_j = [4\pi/(3N_{\text{ngb}})]^{1/3} h_j$  the gas cell effective size.<sup>4</sup> For all the neighbours not fulfilling these criteria, instead, we assume that the momentum  $\Delta \mathbf{p}'_j$  has been already converted into turbulent motion, and has finally decayed into thermal energy, which is added to  $\Delta U$  as  $\Delta E_{\text{turb},j} = |\Delta \mathbf{p}'_j|^2 / (2m_j^{\text{new}})$ .

### 3 BASIC TEST OF THE SCHEME: THE SINGLE SN CASE

We now test the ability of the mechanical feedback model to reproduce the terminal momentum of the SN bubble expansion at different mass resolutions. The setup of the simulations is an homogeneous box of arbitrary size, where particles of mass  $m_i$  (i.e. the mass resolution) are randomly distributed using a Monte Carlo sampling. This is a better choice compared to a regular grid, because it mimics the irregular distribution in less idealised simulations, and also highlights how small numerical density fluctuations do not affect our conclusions. Self-gravity is switched off, and we include radiative cooling and molecular hydrogen ( $\text{H}_2$ ) chemistry using the model described in [Lupi et al. \(2018\)](#)

(4.4b) in [Cioffi et al. \(1988\)](#) for solar-metallicity gas,  $T = 10^4 \text{ K}$ , and  $\beta = 1$ , where  $\beta$  marks the time at which the merging begins. Nevertheless, the exact value for  $R_{\text{max}}$  does not significantly affect the results (see Appendix A).

<sup>4</sup> With our default choice for the kernel, i.e. the cubic spline,  $L_j \approx 0.5h_j$ .

for solar-metallicity gas. To model a SN explosion, we inject  $10^{51}$  erg, together with  $10M_\odot$  of mass, but we do not inject metals, to prevent the change in metallicity, hence the change in the cooling rates. After the SN bubble has reached the momentum-conserving phase, we measure the radial momentum of the expanding gas, and we compare it with the analytic formulae.

The results are shown in Fig. 2 at  $t = 1.0$  Myr for two different densities, i.e.  $n_{\text{Htot}} = 1$  and  $100\text{ cm}^{-3}$  (in the inset). As a comparison, for the  $1\text{ cm}^{-3}$  case only, we also report the fully thermal model (as a green dot-dashed line with the green pentagons), where we inject  $10^{51}$  erg/SN as thermal energy only, and the delayed-cooling model (as a red dashed line with the red circles), where, in addition, we shut off radiative cooling for the survival time of the blast-wave  $t_{\text{max}} = 10^{6.85} E_{51}^{0.32} n_{\text{Htot}}^{0.34} \tilde{P}_{04}^{-0.70}$  yr, where  $\tilde{P}_{04} = 10^{-4} P_0 k_B^{-1}$ , with  $P_0$  the ambient pressure and  $k_B$  the Boltzmann constant (Stinson et al. 2006). The mechanical feedback implementation is well in agreement with the analytic formula at all mass resolutions, up to  $m_j = 10^6 M_\odot$ . Nevertheless, at this very low resolution, the ISM structure, as well as single SN events, are not properly resolved, hence simpler models should be employed in this case (see, e.g. Springel & Hernquist 2003; Vogelsberger et al. 2014; Schaye et al. 2015). The thermal injection model, instead, is very sensitive to resolution, and the terminal momentum drops when the cooling radius is not resolved, because of the overcooling problem. On the other hand, the delayed-cooling model tends to overestimate the terminal momentum at low resolution (approaching the energy-conserving solution). At higher density, the mechanical feedback model still reproduces the terminal momentum very accurately over the entire range of mass resolutions we investigated. This also demonstrates that the model works properly in different density regimes, both at the high densities typical of the sites of SF and at those of the ISM.

#### 4 THE ISOLATED GALAXY CASE: MECHANICAL VERSUS DELAYED-COOLING SUPERNOVA FEEDBACK

We briefly summarise here the sub-grid model we employ in our isolated galaxy simulations. The chemical network and cooling/heating processes are the same as in Lupi et al. (2018), and include non-equilibrium chemistry for 9 primordial species, with  $H_2$  formation via  $H^-$  associative detachment and on dust (see Bovino et al. 2016, for details), an extragalactic ultraviolet (UV) background following Haardt & Madau (2012), and metal cooling look-up tables obtained with Cloudy (Ferland et al. 2013) and tabulated by Shen et al. (2013). Stellar radiation is implemented by collecting all the stellar sources in the gravity tree, and using the total luminosity in the tree nodes when the particles are far away, in a similar fashion to the gravity computation. This approach corresponds to model (b) in Lupi et al. (2018), and showed the best agreement with on-the-fly radiative transfer simulations.

Compared to our previous study, we slightly modify here the SF prescription, to take into account the pressure support when we approach transonic/subsonic regime, fol-

lowing a similar approach to Semenov et al. (2017). Our SF prescription is based on the theoretical studies of turbulent magnetised clouds by Federrath & Klessen (2012). The main assumption in the model, calibrated against simulations and observations, is that the gas follows a Log-Normal density distribution, described by two main quantities, the mean density  $\rho_0$  and the width of the corresponding gaussian distribution  $\sigma_s = \ln(1 + b^2 \mathcal{M}^2)$ , where  $b$  accounts for the ratio between solenoidal and compressive modes. In our case, we assume a statistical mixture of the two modes, which gives  $b = 0.4$ . By averaging the SF rate over the density distribution, we get the net SF efficiency  $\varepsilon$  as

$$\varepsilon = \frac{\varepsilon_\star}{2\phi_t} \exp\left(\frac{3}{8}\sigma_s^2\right) \left[ 1 + \operatorname{erf}\left(\frac{\sigma_s^2 - s_{\text{crit}}}{\sqrt{2}\sigma_s^2}\right) \right], \quad (18)$$

where  $\varepsilon_\star = 0.5$  is the local SF efficiency to match observations (Heiderman et al. 2010),  $1/\phi_t = 0.49$  is a fudge factor to take into account the uncertainty in the free-fall time-scale, and  $s_{\text{crit}} = \ln(\rho_{\text{crit}}/\rho_0)$ , with  $\rho_{\text{crit}}$  the minimum density for SF within the cloud. In this variant of the prescription, we slightly change our implementation as follows:

- we replace the velocity dispersion  $\sigma_v$  in the definition of the virial parameter with the effective energy support against gravitational collapse, i.e.  $\sigma_{\text{eff}} = \sqrt{\sigma_v^2 + c_s^2}$ , where  $c_s$  is the sound speed, obtaining

$$\alpha_{\text{vir}} = \frac{5\sigma_{\text{eff}}^2 L}{6GM_{\text{cloud}}} = \frac{5(\sigma_v^2 + c_s^2)L}{6GM_{\text{cloud}}}, \quad (19)$$

where  $L$  is the cloud diameter (assumed to be the grid-equivalent cell size) and  $M_{\text{cloud}}$  is the particle mass. Assuming the cloud is spherical with  $M_{\text{cloud}} = 4\pi/3\rho_{\text{gas}}(L/2)^3$ , we can rewrite  $\alpha_{\text{vir}}$  as

$$\alpha_{\text{vir}} = \frac{5[\|\nabla \otimes \mathbf{v}\|^2 + (c_s/L)^2]}{\pi G \rho_{\text{gas}}}, \quad (20)$$

where  $\sigma_v = L\|\nabla \otimes \mathbf{v}\|$ . Thanks to the addition of the sound speed to the virial parameter, the SF is self-consistently reduced when we approach a Mach number  $\mathcal{M} = 2$ , a regime where the sound speed can play a non-negligible role in counteracting the gravitational collapse.

- in Lupi et al. (2018), the velocity dispersion was computed using the slope-limited velocity gradients. While the slope-limiting procedure is fundamental for the stability of the Riemann solver, it is undesirable here, since it can artificially produce zero velocity dispersion, preventing some gas particles from forming stars, and creating long-lived dense clumps.<sup>5</sup> In our new variant, we use the ‘real’ gradient, before applying the slope-limiting procedure.

As for the SN feedback, we employ here two different models: the new mechanical feedback model we introduced in the previous section, and the delayed-cooling prescription already described in Lupi et al. (2018). The stellar evolution model, with the different feedback mechanisms considered (type II/Ia SNe and mass losses from low-mass stars) is the

<sup>5</sup> This effect was not visible in the runs by Lupi et al. (2018), since the delayed-cooling model was able to heat up the gas, dissolving these clumps.

**Table 1.** Simulation suite for the isolated galaxy. In the first column, we report the name of the run, in the second the minimum gas softening, in the third one the stellar particle softening, and in the last one the dark matter particle softening.

Run	$\epsilon_{\text{gas, min}}$	$\epsilon_{\star}$	$\epsilon_{\text{DM}}$
Lmech	10 pc	20 pc	80 pc
Hmech	3 pc	6 pc	40 pc
Hdc	3 pc	6 pc	40 pc

same as in our previous study, with the exception of the SN event distribution. While in the previous study SNe were modelled via continuous injection, here we distribute energy, mass, and metals in discrete events. At every time-step, we compute the number of SNe  $x_{\text{SN}}$  expected to explode according to a Chabrier initial mass function (IMF; Chabrier 2003), with the stellar lifetimes from Hurley et al. (2000). Then, we ‘discretize’  $x_{\text{SN}}$  as  $N_{\text{SN}} = \lfloor x_{\text{SN}} \rfloor + \theta(\{x_{\text{SN}}\} - p)$ , where  $\theta$  is the Heaviside step function and  $p$  is a uniformly generated random number between 0 and 1. For each type II SN event, we release  $10^{51}$  erg of energy and the IMF-averaged ejecta masses, respectively a total ejecta mass  $M_{\text{ej}} = 15.1452 - M_{\text{NS}} = 13.7452 M_{\odot}$ , with  $M_{\text{NS}} = 1.4 M_{\odot}$  the mass of the remnant neutron star, an oxygen mass  $M_{\text{oxy}} = 1.2403 M_{\odot}$  and an iron mass  $M_{\text{iron}} = 0.10422 M_{\odot}$ . The total metal mass injected per single event corresponds to  $M_{\text{Z}} = 2.09 M_{\text{oxy}} + 1.06 M_{\text{iron}} = 2.7028 M_{\odot}$ . For type Ia SNe, instead, we inject  $10^{51}$  erg,  $M_{\text{ej}} = 1.4 M_{\odot}$ ,  $M_{\text{oxy}} = 0.14 M_{\odot}$ , and  $M_{\text{iron}} = 0.63 M_{\odot}$ , with a total metal mass injected of  $M_{\text{Z}} = 0.9604 M_{\odot}$ . Finally, for low-mass stars, we expect low-velocity winds, hence we neglect the additional momentum of the wind and only distribute the released mass and the initial momentum to the neighbours. During a Hubble time, our prescription is able to recycle 42 per cent of the initial stellar mass (see Kim et al. 2014, and references therein). In order to resolve single SN events in our simulations, we also add a time-step limiter for the stellar particles. For particles younger than 100 Myr, that are dominated by Type II SN events, we limit the time-step to 1/100th of the typical lifetime of a  $40 M_{\odot}$  star, which is in the range  $3 - 5 \times 10^4$  yr. For older particles, instead, we increase this limit to 1/10th of the age of the stellar population.

#### 4.1 Simulation suite

To compare the two SN feedback models, we evolve a Milky Way-like galaxy at  $z = 0.1$  for 500 Myr in isolation. The initial conditions (ICs) are those of the AGORA collaboration (Kim et al. 2016). We initially relax the ICs for 500 Myr adiabatically, to avoid the initial numerical fragmentation due to the initial density fluctuations, and then enable the sub-grid prescriptions implemented, evolving the galaxy for additional 500 Myr. We run two simulations with our new mechanical feedback model, at different mass/spatial resolutions, and one simulation at high resolution with the delayed-cooling model. At the two resolutions, the gas is sampled with  $10^5$  and  $10^6$  particles, respectively. The full suite of simulations is reported in Table 1.

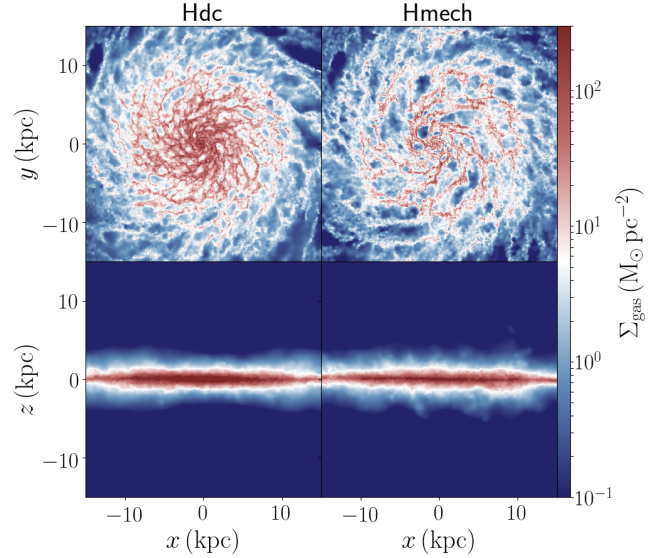


**Figure 3.** Face-on (top panels) and edge-on (bottom panels) views of the galaxy gas surface density at  $t = 500$  Myr for Hmech (right-hand panels) and Hdc (left-hand panels). Because of the lower SFR in Hdc, more gas has remained in the galaxy, producing an overall higher gas density. Nevertheless, the density contrast is larger in Hmech (face-on view), where we observe low-density cavities surrounding high-density SF regions, whereas Hdc exhibits a smoother density distribution. Observed edge-on, the dense disc in Hmech is slightly thinner than that in Hdc, although the low-density gas above and below the disc is very similar in the two runs.

## 5 RESULTS

### 5.1 Delayed-cooling versus mechanical feedback

We discuss now how the galaxy ISM and the SF evolve with the two SN feedback models, by comparing the fiducial simulations, Hmech and Hdc, at the end of the run ( $t = 500$  Myr).

#### 5.1.1 Gas distribution

First, we show in Fig. 3 a qualitative comparison of the gas surface density of the galaxy, face-on and edge-on. The Hdc run is reported in the left-hand panels, whereas Hmech is in the right-hand ones. Hdc shows a higher gas density than Hmech in the central 10 kpc, because of the higher SFR in Hmech which consumed a larger fraction of the available gas (see Fig. 9). Nonetheless, the pressurising effect of the cooling shut-off makes the gas distribution in Hdc slightly smoother than in Hmech, where very high-density SF sites are instead surrounded by the low-density cavities carved by SNe. The edge-on view shows that the dense region of the disc in Hdc is slightly thicker than in Hmech, because of the pressurising effect of the delayed-cooling SN feedback, which keeps the gas hotter. This can be clearly seen in Fig. 4, where we show the vertical surface density profile, obtained as the surface density of the gas within a cylinder of 2 kpc radius at the centre of the galaxy, binned along the  $z$  axis. To remove the discrepancy coming from the different amount

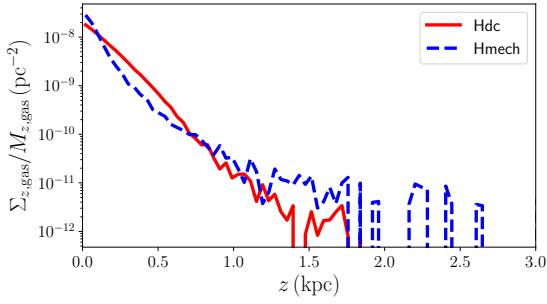


**Figure 4.** Vertical surface density profile at  $t = 500$  Myr for Hdc (red solid) and Hmech (blue dashed), computed within a cylinder of 2 kpc radius around the galaxy centre, normalised to the total gas mass in the cylinder. The pressurising effect of the delayed-cooling prescription makes the disc in Hdc slightly thicker than in Hmech. Although the actual vertical profile changes with time because of SNe, the intrinsic difference between the two models is preserved.

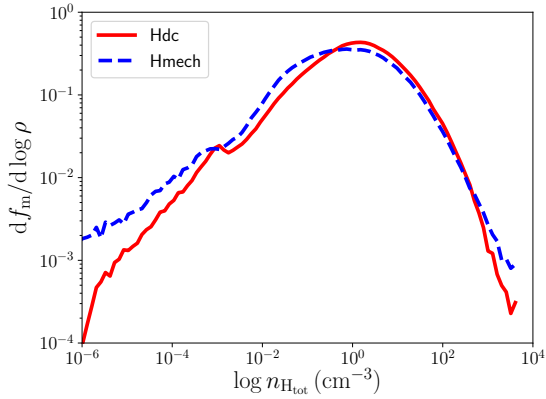


**Figure 5.** Gas mass distribution as a function of total hydrogen nuclei density for Hmech (as a blue dashed line) and Hdc (as a red solid line) at  $t = 500$  Myr, normalised to the total gas mass available. The two profiles show a similar distribution, but with a mild offset to lower densities in Hmech compared to Hdc, and a much more important low-density tail (due to the gas outflows powered by SNe). Although not shown, we repeated the comparison at different times, and the results do not change significantly.

of available gas, the profiles are normalised to the total gas mass  $M_{z, \text{gas}}$  within the cylinder.

Fig. 5 shows the gas mass distribution within the galaxy. We plot the gas mass fraction  $f_m = m_{\text{gas}}/M_{\text{gas}}$  as a function of  $n_{\text{H,tot}}$ , where  $M_{\text{gas}}$  is the total residual gas mass in the galaxy. We binned the gas particles in logarithmically spaced density bins 0.1 decades wide. The gas follows a generally similar distribution, described by a Log-Normal profile at high density and a power-law tail at low density. Nevertheless, some differences can be clearly observed. The amount of gas in the ISM ( $n_{\text{H,tot}} \gtrsim 1 \text{ cm}^{-3}$ ) is slightly lower in Hmech than in Hdc, because of the stronger effect of the mechanical SN feedback which completely destroys the SF clouds, producing strong outflows. This gas is indeed found at much lower densities ( $n_{\text{H,tot}} < 10^{-3} \text{ cm}^{-3}$ ), in the power-law tail, where we observe differences of up to one order of magnitude between the two runs.

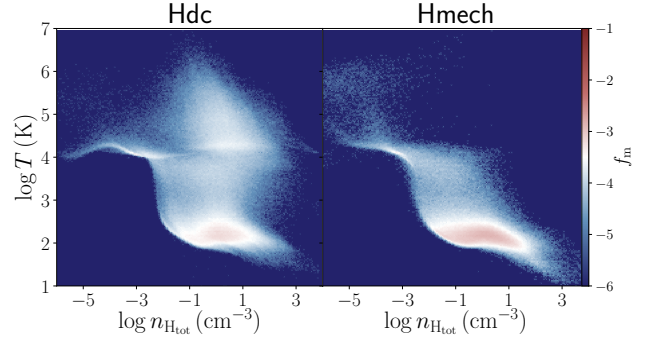


**Figure 6.** Density–temperature diagram for Hmech (as a blue dashed line) and Hdc (as a red solid line) at  $t = 500$  Myr. At densities typical of the ISM and SF regions, Hdc can keep the gas hot (above  $10^4$  K), spreading the gas over 4–5 orders of magnitude in temperature, whereas Hmech allows it to cool down, as it should naturally do.

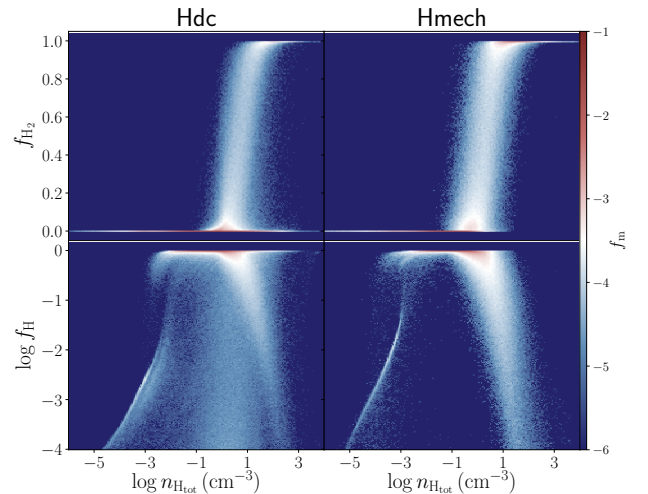


**Figure 7.** Atomic and molecular hydrogen abundances for Hdc (left-hand panels) and Hmech (right-hand panels), as a function of  $n_{\text{H,tot}}$ . The colour map corresponds to the gas mass fraction  $f_m$ . Hmech exhibits a larger amount of  $H_2$  (2.5 times the mass in Hdc), because of the typically lower temperature of the gas compared to Hdc, where gas is more efficiently heated up by SNe, and the high density tail of atomic/ionised hydrogen in Hdc is not visible anymore in Hmech. As for the H abundance, instead, Hmech shows almost no  $H^+$  for  $0.01 \text{ cm}^{-3} \lesssim n_{\text{H,tot}} \lesssim 1.0 \text{ cm}^{-3}$ , while Hdc, thanks to the cooling shut-off, keeps part of this gas hot and ionised.

In Fig. 6, we report the density–temperature diagram of the gas for the same two runs (Hmech in blue and Hdc in red), where the colour map corresponds to the mass fraction  $f_m$ . In Hdc, SNe keep the gas hot, even at densities where it should normally quickly cool down, spreading the gas temperature distribution over 4–5 orders of magnitude. In Hmech, instead, the gas is pushed away by SNe (when the cooling radius is not resolved), getting warmer as it moves to lower densities where the optical depth is lower and it can be

heated up and ionised by local (and extragalactic) stellar radiation. This results in a large fraction of gas remaining cold (below  $10^4$  K) at all densities above  $n_{\text{Htot}} = 10^{-2} \text{ cm}^{-3}$ , where the gas shielding from the extragalactic UV background becomes important.

The different temperature distribution of the gas can have important effects on the chemical state of the gas. To assess the dependence of the distribution on the SN feedback model used, we compare in Fig. 7 the mass fraction of molecular hydrogen  $x_{\text{H}_2}$  (top panels) and atomic hydrogen  $x_{\text{H}}$  (bottom panels) as a function of  $n_{\text{Htot}}$ .  $\text{H}_2$  is 2.5 times more abundant in Hmech (top panels), because of the typically lower temperature of the gas, and the tail of atomic/ionised hydrogen above  $10 \text{ cm}^{-3}$  observed in Hdc (top-left panel), due to the warm/hot gas heated up by SNe, has disappeared in Hmech (top-right panel). As for H, instead, the density interval  $0.01 \text{ cm}^{-3} \lesssim n_{\text{Htot}} \lesssim 1 \text{ cm}^{-3}$  is completely devoid of ionised gas (corresponding to  $f_{\text{H}} \ll 0.1$ ) in Hmech, unlike in Hdc.

Finally, we compare the  $\text{H}_2$  column density with observations of the Milky Way disc and halo (solar metallicity). We compute the column density of both atomic and molecular hydrogen, respectively  $N_{\text{H}}$  and  $N_{\text{H}_2}$ , in a cylinder of 20 kpc radius and 2 kpc height along 25 randomly distributed lines of sight. We report in Fig. 8 the logarithmic  $\text{H}_2$  column density fraction as a function of the total logarithmic column density. The results are binned in 200 log-spaced bins along both axes, where the colour coding represents the point density in each bin. The blue squares refer to the Milky Way disc data by Wolfire et al. (2008), and the green diamonds to the Milky Way halo from the FUSE survey. Both runs agree very well with observations across the entire available data range, with mild differences consistent with those discussed above. In particular, Hmech shows the best agreement, because of the larger fraction of cold gas (hence  $\text{H}_2$ ) compared to Hdc, where the intermediate-density gas kept hot by SNe reduces the  $\text{H}_2$  content. This results in Hmech being able to reach the fully molecular regime, unlike Hdc.

### 5.1.2 The star formation history and the Kennicutt–Schmidt relation

To assess how effective our mechanical feedback model is in suppressing SF, we show in Fig. 9 the SF rate in the Hmech (blue dashed) and Hdc (red solid) runs, estimated by sampling the stellar mass formed in bins of 10 Myr. In the first few tens of Myr, radiative cooling removes the vertical pressure support from the disc, making it collapse vertically. This triggers an initial burst of SF of up to a few tens of  $M_{\odot} \text{ yr}^{-1}$ , and a subsequent burst of SN explosions. With the delayed-cooling model, SNe heat up the gas and keep it hot, increasing the pressure support and reducing  $\mathcal{M}$ . This turns out in a very quick suppression of the SF down to less than  $1 M_{\odot} \text{ yr}^{-1}$ . Then, the galaxy settles in a self-regulated state, with a steady SFR in the range  $1 - 2 M_{\odot} \text{ yr}^{-1}$ . With the mechanical feedback model, instead, the gas is swept away from the SF sites, but not heated up significantly. Because of the kick imparted by SNe and the low temperature of the gas, strong shocks occur within the ISM, producing new stars and, subsequently, new SNe. As a consequence, in Hmech, we observe a steady decay instead of an abrupt suppression, with the galaxy taking more time to settle in a self-regulated

state. This also results in more gas being consumed by SF than in Hdc, in agreement with previous studies like Rosdahl et al. (2017) and Smith et al. (2018).

Observations of low-redshift galaxies clearly demonstrated that a correlation exists between the SFR and the gas surface densities in galaxies (KS hereon; Schmidt 1959; Kennicutt 1998), with a power-law scaling as  $\dot{\Sigma}_{\star} \propto \Sigma_{\text{g}}^{1.4}$ . Recently, the effort made to collect a large sample of data has allowed us to improve the constraints on this relation, and to show that a tight correlation exists between the SFR and the molecular gas content, whereas almost no correlation exists with the abundance of atomic hydrogen (Bigiel et al. 2008). In Fig. 10, we compare the ability of the two SN feedback models in reproducing the KS relation, in both total gas ( $\text{H} + \text{H}_2$ , left-hand panel) and molecular gas ( $\text{H}_2$ , right-hand panel) only. The filled contours correspond to observations by Bigiel et al. (2008) (green), Bigiel et al. (2010) (red), binned in 0.1 decade wide bins on both axes, and Schrubba et al. (2011) (purple), binned in 0.2 decade wide bins on both axes. The different contour levels correspond to the density of data points in the bins, respectively 2, 5, and 10. To accurately compare the simulated galaxies with observations, we compute the far ultraviolet (FUV) flux of the stellar sources, according to the age and metallicity of each star particle, and we use the relation in Salim et al. (2007) to convert the FUV luminosity into a SFR. We then estimate the density and the SFR in square patches 750 pc wide, with the galaxy seen face-on, and we finally bin the data points along the gas density axis in 0.2 decade-wide bins, reporting the average SFR in each bin, and the standard deviation as the y-axis error bar. In order to exclude poorly sampled bins, we remove all the bins with less than five data points. Hdc (red solid line) agrees well with the observed data, for both total gas and  $\text{H}_2$ , with a small overshooting at the highest densities. Hmech (blue dashed line), on the other hand, exhibits a higher SFR in the total gas, with a factor of a few difference relative to Hdc. However, in the molecular relation (right-hand panel), both models well match the observations, with Hmech almost perfectly overlapping Hdc. This suggests that, while the KS in total gas can be significantly influenced by the SN feedback model employed, the molecular gas counterpart is more robust to these changes.

### 5.1.3 Outflow properties

Another key aspect to assess the ability of different SN feedback models into regulating SF is the production of outflows. Gas ejected from SNe moves into the halo (in some cases, it can also escape the halo gravitational potential), falling back at later times and triggering a new phase of SF. Galactic outflows are routinely observed in galaxies (Steidel et al. 2010; Heckman et al. 2015), but many properties as the mass outflow rate and the density/temperature state of the gas are not constrained very well. In Fig. 11, we compare the outflow properties for the two SN feedback models, i.e. the mass outflow rate, the mass loading factor  $\beta_{\text{out}} = \dot{M}_{\text{out}}/\dot{M}_{\star}$ , and the outflow velocity. We measure the outflows at 2 kpc (left-hand panels) and 20 kpc (right-hand panels) from the galactic plane, selecting the gas particles with  $v_z \cdot z > 0$ , with  $v_z$  the vertical velocity, in a slab with  $\Delta z = 0.2$  kpc. This corresponds to the gross outflow (neglecting any inflowing



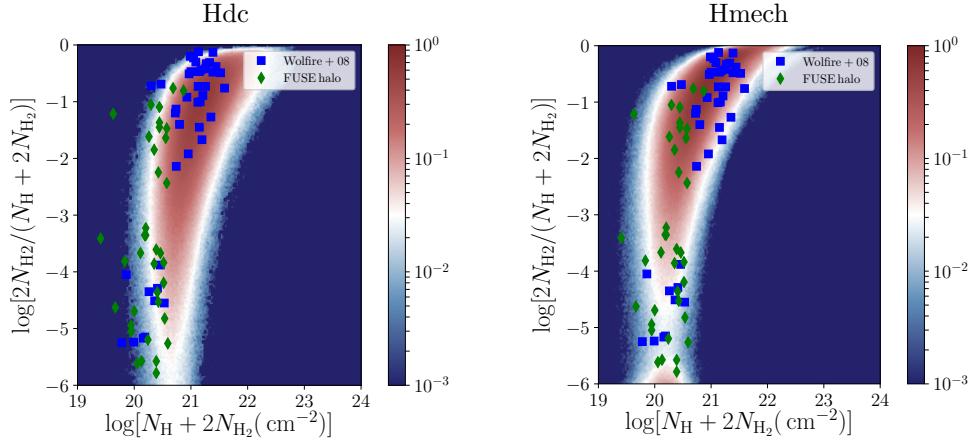


**Figure 8.**  $H_2$  column density fraction in Hdc (left-hand panel) and Hmech (right-hand panel) at  $t = 500$  Myr, compared with local observations of molecular clouds in the Milky Way disc and halo, and in the Large Magellanic Cloud. Our simulation results overlap very well with observations across the entire available column density range, with Hmech showing a remarkable agreement. Thanks to the typically lower gas temperatures (a crucial difference with Hdc, where cooling shut-off keeps gas hot above  $n_{\text{Hot}} \sim 0.1 - 1 \text{ cm}^{-3}$ , artificially suppressing  $H_2$  formation),  $H_2$  is significantly more abundant in Hmech, shifting the distribution upwards, allowing it to more easily reach the fully molecular regime.

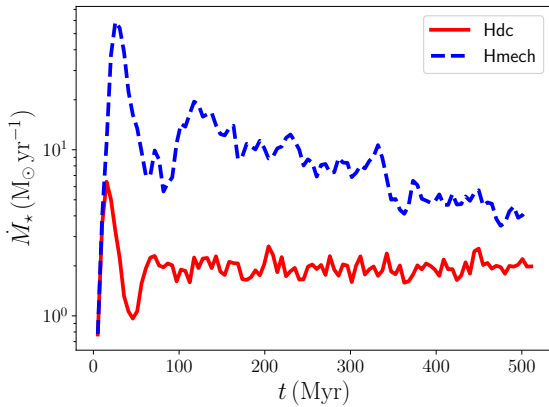


**Figure 9.** SF rate in the Hmech (blue dashed) and Hdc (red solid) runs. After the initial burst of SF, Hdc shows a steady evolution at almost constant SFR of about  $1-2 \text{ M}_\odot \text{ yr}^{-1}$ , due to the high temperature of the gas affected by SN feedback, which does not form stars for long timescales (a few tens of Myr). In Hmech, on the other hand, SNe do not heat the gas up, but sweep it away, triggering strong shocks with the cold ISM and producing new stars. This delays the establishment of a self-regulated equilibrium, and results in more gas being consumed by SF.

gas). The mass outflow rate at 2 kpc (top-left panel) is a factor of a few higher in Hmech than in Hdc. At 20 kpc, the difference is even larger, with Hmech being roughly one order of magnitude higher than Hdc. At late times, when the disc has reached a self-regulated equilibrium, the outflow rate is more similar between the two runs, but significantly low ( $\dot{M}_{\text{out}} \lesssim 10^{-2} \text{ M}_\odot \text{ yr}^{-1}$ ). The situation is more complex for  $\beta_{\text{out}}$ , because of the additional dependence on the SFR. At 2 kpc, the larger outflow rates in Hmech compensate the higher SFRs relative to Hdc, resulting in a comparable  $\beta_{\text{out}} \sim 0.5 - 1$ . At larger distances, instead, Hmech can reach  $\beta_{\text{out}} \sim 10^{-2}$ , in particular during the first 300 Myr, when the SFR is higher, whereas Hdc never exceeds  $\beta_{\text{out}} \sim 5 \times 10^{-3}$ ,

and in many cases the outflow rate is unresolved. In the bottom panels, we show the outflow velocity, computed as

$$\langle v_{\text{out}} \rangle = \frac{\sum_j m_j |v_{j,z}|}{\sum_j m_j}, \quad (21)$$

where  $m_j$  is the  $j$ -th particle mass and the sum is over the particles in the outflow ( $v_z \cdot z > 0$  and  $|z - z_0| < \Delta z$ , with  $z_0$  the distance from the galactic plane). As a reference, we also show the escape velocity<sup>6</sup> from the system, computed from the corresponding height  $z$  above the disc to infinity, as a grey dot-dashed line. Also in this case, at 2 kpc Hmech results in slightly larger outflowing velocities relative to Hdc, within a factor of 2-3, because of the stronger effect of SN feedback. At larger distances, instead, the average outflow velocity is consistent between the runs, with Hdc showing a larger scatter because of the low gas mass involved, hence the under-sampling of the outflow properties. In conclusion, the mechanical feedback appears to be more effective in producing outflows than delayed-cooling, but at the same time it is not as effective in suppressing SF within the galaxy. This suggests that delayed-cooling, despite being empirical, probably mimics additional non-thermal processes which help suppressing SF in galaxies, whereas the mechanical feedback only accounts the ‘thermally driven’ evolution of the bubble. Recent studies have shown that the preprocessing of the ISM in the presence of stellar radiation and young stellar winds can significantly alter the SN evolution, and can result in a larger terminal momentum of the bubble and a more effective suppression of SF. However, this is beyond the scope of this paper and will be investigated in the future.

<sup>6</sup> The escape velocity is computed from the potential in the initial conditions, at the corresponding height above the disc plane and cylindrical radius  $R = 0$ . We do not consider changes in the distribution during the simulation.

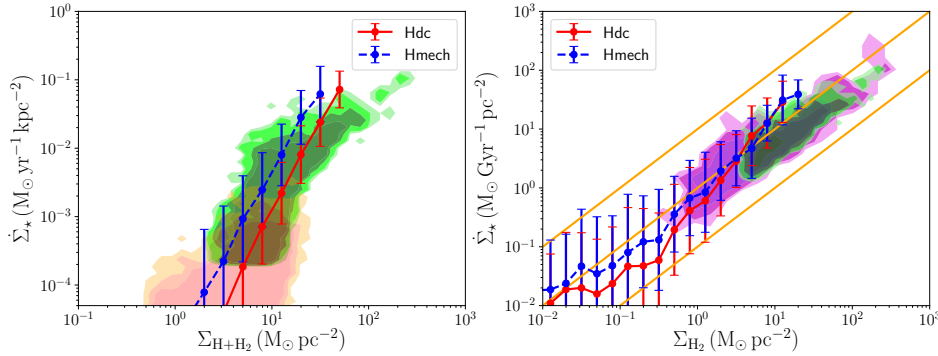


**Figure 10.** KS relation for the Hmech (blue dashed) and Hdc (red solid) runs, in both total gas ( $\text{H}+\text{H}_2$ , left-hand panel) and molecular gas ( $\text{H}_2$ , right-hand panel) only, compared with the observational samples by Bigiel et al. (2008, 2010) and Schrubba et al. (2011). For the simulated data, we show here the average SFR, with its standard deviation  $\sigma$  reported in the vertical error bar. Hdc agrees very well with the observed data in both panels, with only a small overshooting at high densities. In the left-hand panel, the higher SFR of Hmech results in the points being closer to the upper boundary of the observational contours, but still consistent with the observed data. In the right-hand panel, instead, the correlation is better preserved, with Hmech almost overlapping the Hdc results at all densities.

## 5.2 Resolution dependence of the scheme

Now, we assess the resolution dependence of the mechanical feedback model, comparing Lmech and Hmech.

In Fig. 12, we report the vertical profile of the galaxy at different resolutions, following the same approach described in Fig. 4. In Lmech, the lower resolution, resulting in lower densities and larger volumes associated with each gas particle, the impact of SN explosions is slightly stronger than in Hmech, and produces a slightly thicker disc. In Fig. 13, we compare the gas mass distribution as a function of density. In this case, the two runs show a very similar behaviour, although Lmech peaks at slightly lower densities than Hmech. An almost perfect overlap is observed for  $n_{\text{H}_{\text{tot}}} \lesssim 0.1 \text{ cm}^{-3}$ . At higher densities, instead, the larger particle mass and the poorer sampling of the velocity dispersion in Lmech result in a slightly more efficient SF already around  $10 \text{ cm}^{-3}$ , preventing the gas from collapsing further to reach the highest densities observed in Hmech. In addition, SNe become more effective when they explode in lower density environments, hence further reducing the gas in this density interval. Although not shown here, we find that the density–temperature diagrams are in very good agreement, except for the poorer sampling in Lmech, whereas the  $\text{H}_2$  abundance is moderately lower, consistent with the slightly lower densities observed.

By comparing the SF history in the two runs in Fig. 14, we can notice that Lmech exhibits a slightly lower SFR than Hmech in the first 250 Myr, consistent with the fact that i) the maximum density achieved is typically lower than in Hmech, thus reducing the initial burst of SF, and ii) SN events are more effective in sweeping away the gas when the density around the star is lower. Nevertheless, this difference almost vanishes as the simulation proceeds, resulting in a comparable SFR with small fluctuations.

In Fig. 15, we show the KS relation for Hmech (blue stars) and Lmech (red dots) in both total gas and  $\text{H}_2$  only. In the left-hand panel, Lmech is slightly lower than Hmech, but the two runs always agree within the error bars. This difference is probably due to the poorer sampling in Lmech, that increases the scatter of the distribution, mildly affecting

the mean value. In the right-hand panel, instead, the agreement between Hmech and Lmech is almost perfect. These results suggest that the KS relation, especially the  $\text{H}_2$ -only counterpart, is robust against resolution.

Finally, we compare the outflow properties at different resolutions in Fig. 16. Closer to the disc plane, the outflows are a bit stronger in Lmech (top-left and middle-left panels), because of the lower resolution and the SNe interacting with farther away neighbours, but. Nevertheless, the average velocity is the same in the two runs. At larger distances, instead, the two runs agree well (right-hand panels), except for the last 50 Myr, when the outflows weaken, worsening the sampling of the outflow rate in Lmech, and producing a moderate discrepancy. An additional difference due to the different volume sampling is the scattering during the evolution, which is much larger in Lmech compared to Hmech.

## 6 DISCUSSION AND CONCLUSIONS

We introduced here a new physically motivated SN feedback model able to deposit the right amount of energy and momentum into the ISM, according to the results of high-resolution, small-scale simulations. After validating the model using isolated SN explosions in a uniform medium at different resolutions, we applied the model to a Milky Way-like galaxy at  $z \sim 0.1$  in isolation, to assess its ability to reproduce the observed correlation between SF and  $\text{H}_2$ . We compared this new model with the delayed-cooling SN feedback model employed in Lupi et al. (2018), which showed very good agreement with observations (see also Capelo et al. 2018), despite the unphysical temperature of the gas kept hot by SNe, and we also tested the resolution dependence of the model. We summarise here our findings:

- Terminal momentum in a uniform medium: the mechanical feedback model almost perfectly reproduces the terminal momentum of a single SN event, independent of resolution. The delayed-cooling prescription, on the other hand, overestimates it by up to an order of magnitude, at low resolu-

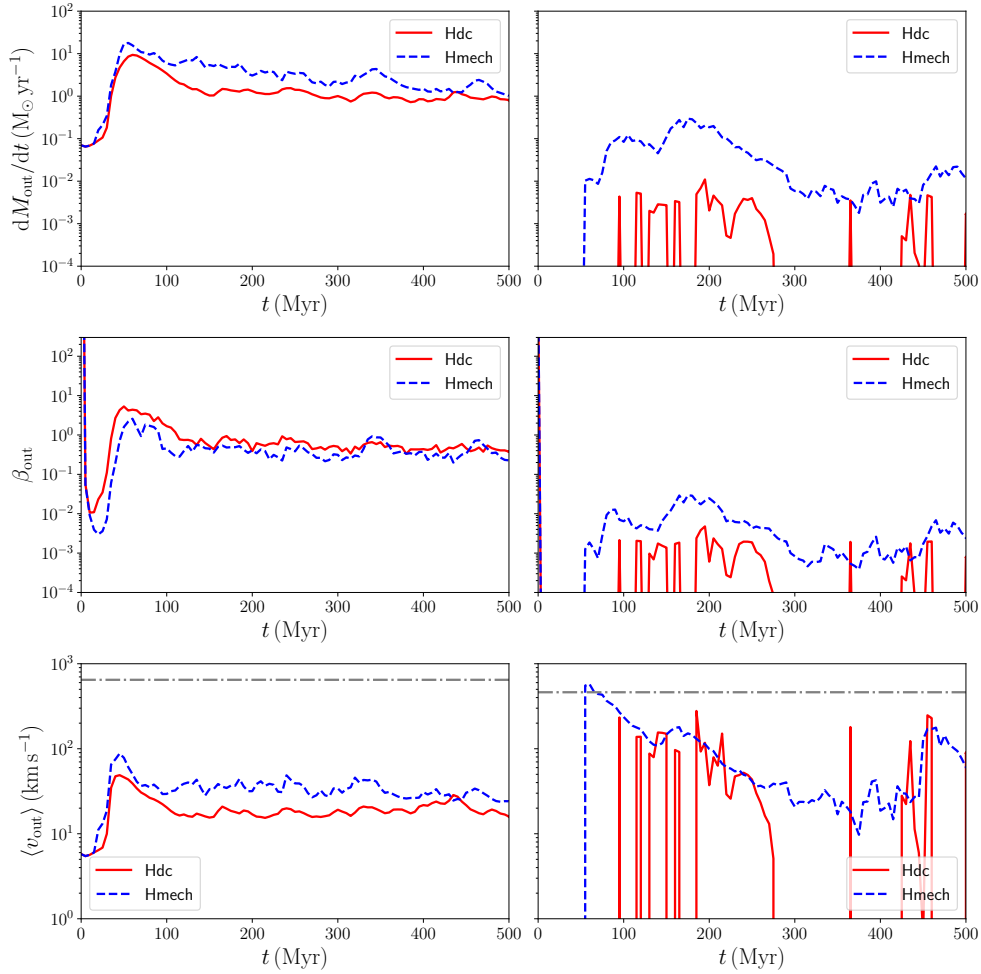


**Figure 11.** Outflow properties for the Hmech (blue dashed) and Hdc (red solid) runs, at 2 kpc (left-hand panels) and 20 kpc (right-hand panels) from the galactic disc plane. In the top panels, we show the mass outflow rate, in the middle panels the  $\beta_{\text{out}}$  parameter, and in the bottom panels the outflow mean velocity. The dot-dashed lines in the bottom panels correspond to the maximum escape velocity from the disc at  $z = 2$  kpc (left-hand panel) and  $z = 20$  kpc (right-hand panel), respectively. Hmech is able to produce stronger outflows relative to Hdc. While this effect could in principle be associated with the higher SFR in Hmech, consistent with the  $\beta_{\text{out}}$  measured in Hdc at 2 kpc, the results at 20 kpc clearly demonstrate that this is not the case. Indeed, Hdc is very inefficient at producing outflows up to 20 kpc, with mass rates and  $\beta_{\text{out}}$  roughly one order of magnitude lower than in Hmech.

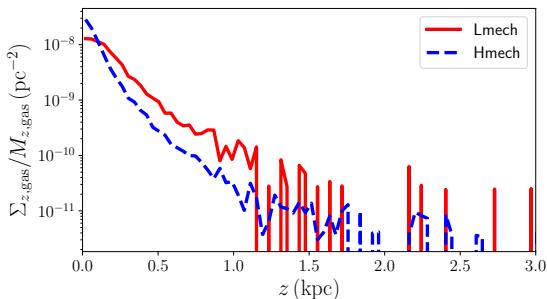


**Figure 12.** Vertical surface density profile at  $t = 500$  Myr for Lmech (red solid) and Hmech (blue dashed). Edge-on, the disc in Lmech is slightly thicker than in Hmech, because of the typically larger volume per particle and the subsequent stronger impact of SN feedback onto the gas farther away from the disc, where the densities are typically lower.

tion, because of the cooling shut-off that draws the evolution closer to the fully energy-conserving case.

- Model comparison – SF in the galaxy: the delayed-cooling model more effectively suppresses SF, because of the artificial pressurisation of the gas, that completely inhibits SF for some time. On the other hand, the mechanical feedback more effectively sweeps away the gas, but is not able to properly describe the hot, low-density cavity produced, probably resulting in a slightly too high SF rate. Nonetheless, a detailed study of this possibility is beyond the scope of the present study.

- Model comparison – KS relation: the  $H_2$  KS relation and the  $H_2$  column density fraction are consistent between the two models, suggesting that these correlations are reasonably robust against different sub-grid models, as already stated in Lupi et al. (2018) for the SF prescription. On the other hand, the total KS relation is slightly higher in the mechanical feedback run, because of the overall higher SFR relative to the delayed-cooling case.

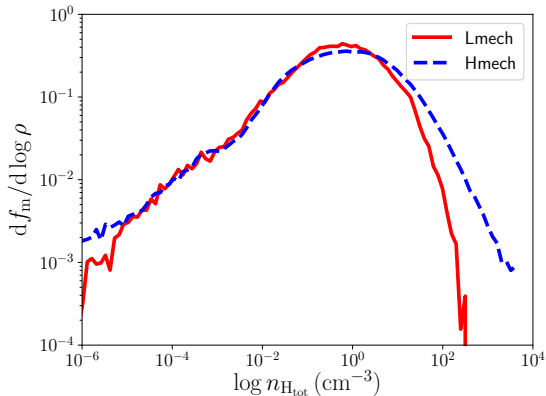


**Figure 13.** Gas mass distribution of Lmech (red solid) with respect to Hmech (blue dashed) at  $t = 500$  Myr. The two profiles are in very good agreement for  $n_{\text{H,tot}} \lesssim 0.1 \text{ cm}^{-3}$ . At higher densities, instead, the poorer sampling of the velocity dispersion and the larger particle masses result in a mild increase of the SFR for  $n_{\text{H,tot}} \sim 10 \text{ cm}^{-3}$ , which prevents the gas from collapsing further.

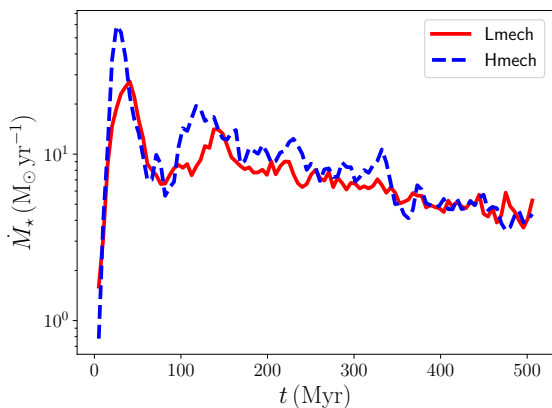


**Figure 14.** SF rate in the Hmech (blue dashed) and Lmech (red solid) runs. Hmech shows a higher initial peak, because of the instantaneous cooling that triggers the vertical collapse of the disc and the fragmentation on smaller scales than in Lmech. Nevertheless, the subsequent SN events realign Hmech with Lmech, resulting in a consistent SFR rate evolution.

- Model comparison – galaxy outflows: the mechanical feedback model drives more massive outflows compared to the delayed-cooling model, especially at larger distances. Closer to the galaxy, instead, the two models agree very well, with a consistent  $\beta_{\text{out}} \sim 1$ . In all the cases, the outflows never exceed the escape velocity from the halo, hence resulting in galactic fountains rather than proper outflows.

- Resolution dependence: the mechanical feedback model is only mildly resolution-dependent. In particular, in the low-resolution run, the KS relation in total gas is slightly offset, but this is probably due to the coarser resolution that results in a larger scatter of the binned properties, and the outflows close the galactic plane (2 kpc) are slightly higher, because of the typically larger volumes of each cell and the SN–gas interaction that extends to larger distances from the disc plane. All other properties, instead, are consistent between the two resolutions, with stronger fluctuations in the

low-resolution case due to the poorer sampling of the gas properties.

A possible limitation of the study is the overshooting of the  $\text{H}_2$  KS relation in both SN feedback models. As already stated in Lupi et al. (2018), this could be related to (i) the fact that, at high densities, the SF prescription converts gas into stars very quickly, removing all the molecular hydrogen available for the converted gas particle, hence reducing its surface density, or (ii) to the numerical diffusion close to the resolution limit which slightly reduces the turbulent support of the gas. A possible solution to avoid the second issue is to include a sub-grid model for the turbulent cascade, as in Semenov et al. (2017). Another limitation, that could also explain the higher SFR in the mechanical feedback runs, is the lack of additional feedback processes like HII regions, young stellar winds, and cosmic rays, that could help provide additional energy/pressure able to more efficiently suppress SF. In the delayed-cooling runs, instead, the empirical choice of shutting off radiative cooling could probably mimic (despite not in a completely physical fashion) these additional processes not present in the mechanical feedback model. An alternative explanation for the too high SFR in the mechanical feedback model could be that the momentum injected by the model is too low compared to reality (see, e.g. Keller et al. 2014; Gentry et al. 2017), i.e. the shocks in the swept-away gas should be stronger and the gas heating more effective. However, a thorough investigation of these effect is beyond the scope of this study.

Concluding, despite the intrinsic differences, both models are reasonably consistent with each other, and are able to reproduce many galaxy properties in a similar way. However, the mechanical feedback, despite not being as effective as the delayed cooling in suppressing the SF, better reproduces the thermo-chemical state of the gas, the  $\text{H}_2$  column densities observed, and is also able to drive more powerful outflows. Although further investigations are certainly necessary to fully assess the limitations of the mechanical feedback model, its physical motivation and ability to accurately reproduce the terminal momentum independent of resolution represent a step forward compared to the empirical delayed cooling mode. Thanks to the general effort of the community in improving the sub-grid modelling, mechanical feedback, coupled with other state-of-the-art prescriptions for processes like SF, chemistry, and enrichment will definitely help us to better understand how galaxies self-regulate during their evolution.

## ACKNOWLEDGEMENTS

We thank Marta Volonteri, Massimo Dotti and Pedro R. Capelo for useful discussions and suggestions. We thank Sijing Shen for having provided the metal cooling table described in Shen et al. (2010, 2013). AL acknowledges support from the European Research Council (Project No. 267117, ‘DARK’; Project no. 614199, ‘BLACK’). This work was granted access to the High Performance Computing resources of CINES under the allocations x2016046955, A0020406955, and A0040406955 by GENCI, and it has made use of the Horizon Cluster, funded by Institut d’Astrophysique de Paris, for the analysis of the simulation results.

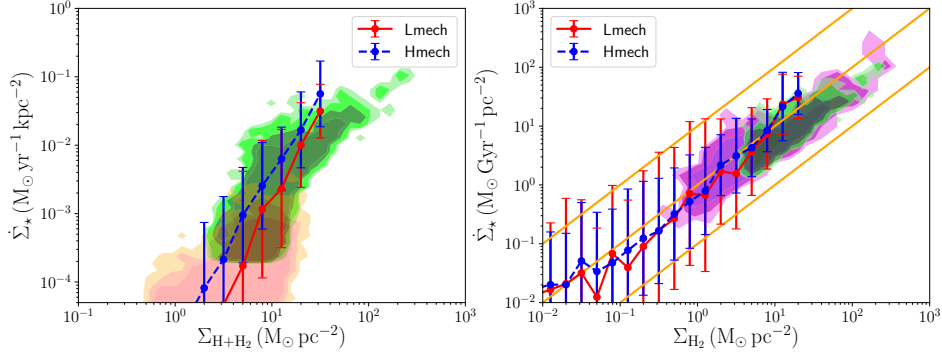


**Figure 15.** KS relation for the Hmech (blue dashed) and Lmech (red solid) runs, in both total gas ( $\text{H}+\text{H}_2$ , left-hand panel) and molecular gas ( $\text{H}_2$ , right-hand panel) only. In the left-hand panel, Lmech is slightly below Hmech, but the scatter is much larger, and completely encompasses the Hmech data. In the right-hand panel, on the other hand, the agreement is almost perfect. These results suggest that the KS relation, in particular the  $\text{H}_2$ -only counterpart, is robust against resolution.

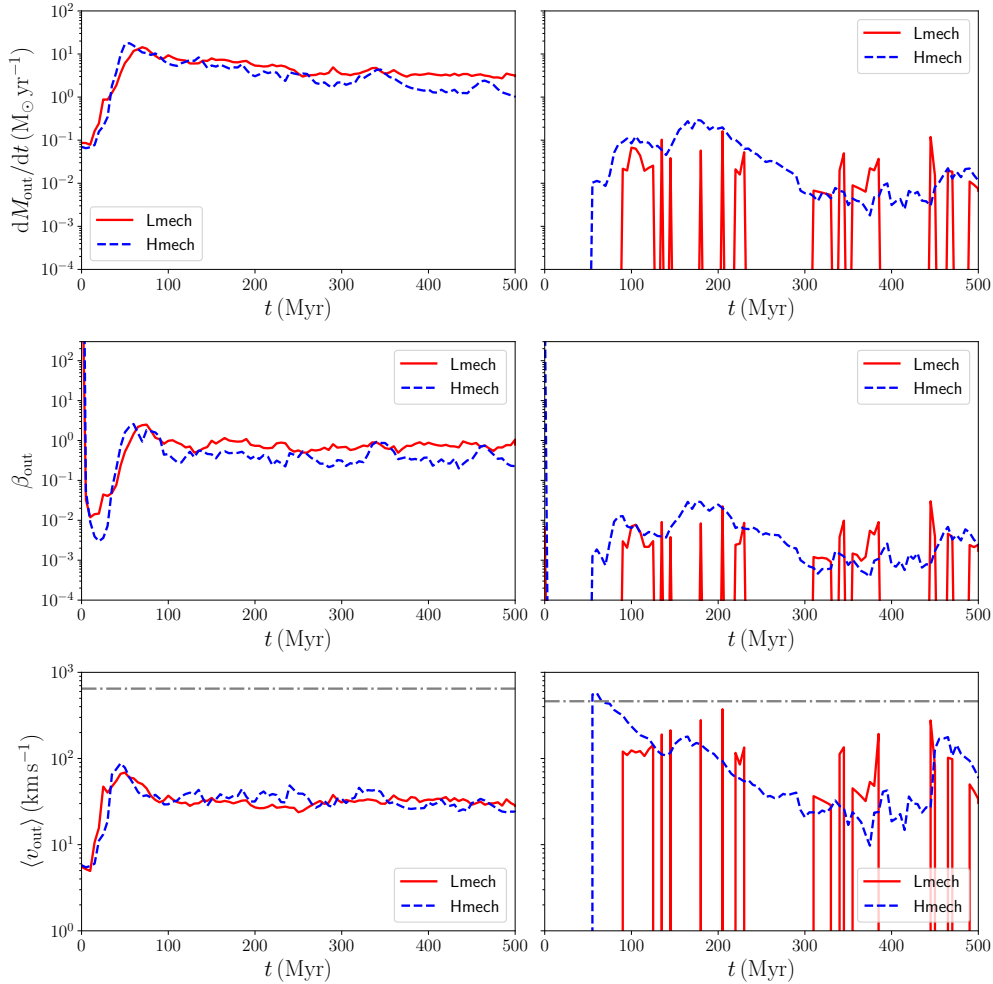


**Figure 16.** Same as Fig. 11, for the Hmech (blue dashed) and Lmech (red solid) runs. Closer to the disc plane, the coarser resolution of Lmech favours the SN interaction with the gas further away and at slightly lower densities, resulting in mildly stronger outflows. However, the typical velocity of the gas is not affected by the resolution. On the other hand, at larger distances, the resolution effects become less important, and two runs show a good agreement, but with stronger fluctuations (due to the poorer mass resolution) in Lmech relative to Hmech. At later times, the net weakening of the outflows results in an even stronger under-sampling for Lmech, and a moderate discrepancy between the two runs arises.

## REFERENCES

- Bigiel F., Leroy A., Walter F., Brinks E., de Blok W. J. G., Madore B., Thornley M. D., 2008, *AJ*, **136**, 2846
- Bigiel F., Leroy A., Walter F., Blitz L., Brinks E., de Blok W. J. G., Madore B., 2010, *AJ*, **140**, 1194
- Bournaud F., Elmegreen B. G., Teyssier R., Block D. L., Puerari I., 2010, *MNRAS*, **409**, 1088
- Bovino S., Grassi T., Capelo P. R., Schleicher D. R. G., Banerjee R., 2016, *A&A*, **590**, A15
- Capelo P. R., Bovino S., Lupi A., Schleicher D. R. G., Grassi T., 2018, *MNRAS*, **475**, 3283
- Chabrier G., 2003, *PASP*, **115**, 763
- Chevalier R. A., 1974, *ApJ*, **188**, 501
- Cioffi D. F., McKee C. F., Bertschinger E., 1988, *ApJ*, **334**, 252
- Dalla Vecchia C., Schaye J., 2012, *MNRAS*, **426**, 140
- Dobbs C. L., Burkert A., Pringle J. E., 2011, *MNRAS*, **413**, 2935
- Federrath C., Klessen R. S., 2012, *ApJ*, **761**, 156
- Ferland G. J., et al., 2013, *Rev. Mexicana Astron. Astrofis.*, **49**, 137
- Geen S., Hennebelle P., Tremblin P., Rosdahl J., 2016, *MNRAS*, **463**, 3129
- Gentry E. S., Krumholz M. R., Dekel A., Madau P., 2017, *MNRAS*, **465**, 2471
- Haardt F., Madau P., 2012, *ApJ*, **746**, 125
- Haid S., Walch S., Naab T., Seifried D., Mackey J., Gatto A., 2016, *MNRAS*, **460**, 2962
- Heckman T. M., Alexandroff R. M., Borthakur S., Overzier R., Leitherer C., 2015, *ApJ*, **809**, 147
- Heiderman A., Evans II N. J., Allen L. E., Huard T., Heyer M., 2010, *ApJ*, **723**, 1019
- Hopkins P. F., 2015, *MNRAS*, **450**, 53
- Hopkins P. F., Cox T. J., Hernquist L., Narayanan D., Hayward C. C., Murray N., 2013, *MNRAS*, **430**, 1901
- Hopkins P. F., et al., 2018a, *MNRAS*, **477**, 1578
- Hopkins P. F., et al., 2018b, *MNRAS*, **480**, 800
- Hurley J. R., Pols O. R., Tout C. A., 2000, *MNRAS*, **315**, 543
- Keller B. W., Wadsley J., Benincasa S. M., Couchman H. M. P., 2014, *MNRAS*, **442**, 3013
- Kennicutt Jr. R. C., 1998, *ApJ*, **498**, 541
- Kim C.-G., Ostriker E. C., 2015, *ApJ*, **802**, 99
- Kim J.-h., et al., 2014, *ApJS*, **210**, 14
- Kim J.-h., et al., 2016, *ApJ*, **833**, 202
- Kimm T., Cen R., 2014, *ApJ*, **788**, 121
- Lupi A., Bovino S., Capelo P. R., Volonteri M., Silk J., 2018, *MNRAS*, **474**, 2884
- Martizzi D., Faucher-Giguère C.-A., Quataert E., 2015, *MNRAS*, **450**, 504
- McKee C. F., Ostriker J. P., 1977, *ApJ*, **218**, 148
- Navarro J. F., White S. D. M., 1993, *MNRAS*, **265**, 271
- Rosdahl J., Schaye J., Dubois Y., Kimm T., Teyssier R., 2017, *MNRAS*, **466**, 11
- Salim S., et al., 2007, *ApJS*, **173**, 267
- Schaye J., et al., 2015, *MNRAS*, **446**, 521
- Schmidt M., 1959, *ApJ*, **129**, 243
- Schruba A., et al., 2011, *AJ*, **142**, 37
- Sedov L. I., 1959, *Similarity and Dimensional Methods in Mechanics*
- Semenov V. A., Kravtsov A. V., Gnedin N. Y., 2017, *ApJ*, **845**, 133
- Shen S., Wadsley J., Stinson G., 2010, *MNRAS*, **407**, 1581
- Shen S., Madau P., Guedes J., Mayer L., Prochaska J. X., Wadsley J., 2013, *ApJ*, **765**, 89
- Smith M. C., Sijacki D., Shen S., 2018, *MNRAS*, **478**, 302
- Springel V., 2005, *MNRAS*, **364**, 1105
- Springel V., 2010, *MNRAS*, **401**, 791
- Springel V., Hernquist L., 2003, in Makino J., Hut P., eds, *IAU Symposium Vol. 208, Astrophysical Supercomputing using*

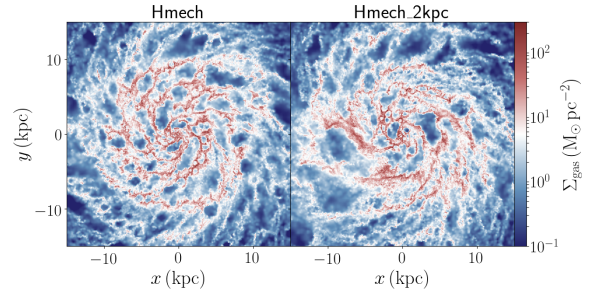


**Figure A1.** Face-on view of the galaxy in Hmech (left-hand panels) and Hmech\_2kpc (right-hand panel) at the end of the simulation, as in Fig. 3. In Hmech\_2kpc, the bubbles are typically larger, because of the larger coupling radius assumed. However, this is only a qualitative aspect, and it does not affect the quantitative evolution of the galaxy.

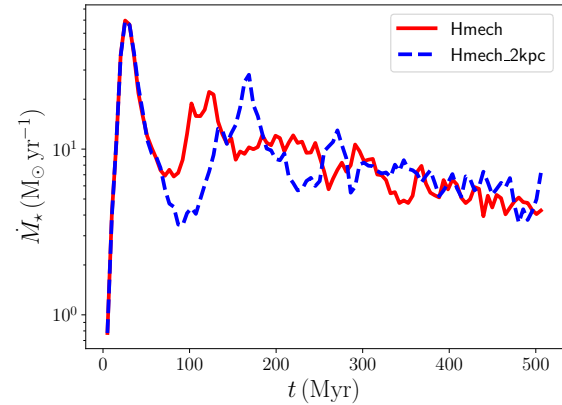


**Figure A2.** SFR of the galaxy in Hmech (solid red) and Hmech\_2kpc (blue dashed). In Hmech\_2kpc, the initial burst is more effective in suppressing the SF, but it only shifts the second SF peak at later times, without significantly changing the final stellar mass (within a few per cent).

- Particle Simulations. p. 273
- Steidel C. C., Erb D. K., Shapley A. E., Pettini M., Reddy N., Bogosavljević M., Rudie G. C., Rakic O., 2010, *ApJ*, **717**, 289
- Stinson G., Seth A., Katz N., Wadsley J., Governato F., Quinn T., 2006, *MNRAS*, **373**, 1074
- Taylor G., 1950a, *Proceedings of the Royal Society of London Series A*, **201**, 159
- Taylor G., 1950b, *Proceedings of the Royal Society of London Series A*, **201**, 175
- Vogelsberger M., et al., 2014, *MNRAS*, **444**, 1518
- Wolfire M. G., Tielens A. G. G. M., Hollenbach D., Kaufman M. J., 2008, *ApJ*, **680**, 384

## APPENDIX A: LIMITER FOR MOMENTUM COUPLING

Here, we discuss our choice of a distance/density limiter for the momentum coupling scheme, by presenting a variant of our mechanical feedback model, that we name ‘Hmech\_2kpc’. In this variant, we couple the momentum obtained from Eq. (16) to all the particles within a distance of 2 kpc from the star, without any check on the density or

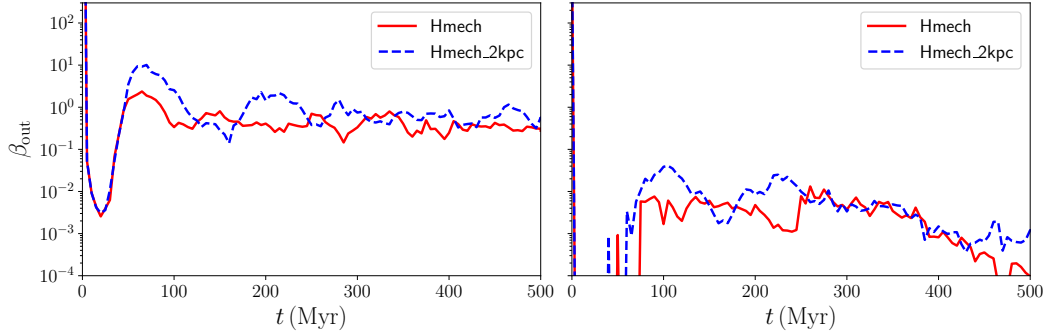


**Figure A3.**  $\beta_{\text{out}}$  at 2 kpc and 20 kpc for Hmech (solid red) and Hmech\_2kpc (blue dashed). In Hmech\_2kpc, the larger coupling radius is able to push the gas more effectively at 2 kpc. However, at these distances from the disc, the exact choice of the maximum radius can play a role, although moderate. At larger distances, instead, this choice is less relevant, as suggested by the very good agreement between the two runs, especially after the first 250 Myr.

on the distance of the effective face. As already stated in Section 2.3, for a very-low density medium, the SN bubble should merge while still in the energy conserving phase. In this case, the solution from Martizzi et al. (2015) is not correct any longer and can artificially enhance the feedback effect. To highlight how important the exact choice for the limiter is, we compare Hmech with Hmech\_2kpc. In Fig. A1, we show a face-on map of the gas in the two runs. Hmech\_2kpc, because of the larger coupling radius, can produce larger bubbles compared to Hmech. However, this does not affect significantly the other galaxy properties. For instance, the vertical profile of the disc is in perfect agreement between the two runs, although not reported. In Fig. A2, we show the SFR evolution for the two runs. We observe different fluctuations, because of the small differences in the coupling, in particular during the initial phases when the galaxy has not reached yet a steady-state evolution. At late times, instead, the two runs agree well. In Fig. A3, instead, we compare  $\beta_{\text{out}}$  for the two runs. At 2 kpc (left-hand panel), Hmech\_2kpc is slightly above Hmech, because of the coupling extending up to larger distances. However, at 20 kpc, this difference becomes negligible, and the agreement between the two runs is almost perfect, with the only exception of a moderate rise in Hmech\_2kpc, following the small SF burst observed close to the end of the run in Fig. A2. The other quantities discussed in the main text are not reported here, for simplicity, because no differences have been observed between the two runs. We can therefore conclude that the exact choice of the limiter does not play a significant role in the galaxy evolution, as long as the value is large enough (for instance, a multiple of the expected merging radius at very low density) to avoid spurious suppression of the feedback.